



Effect of manganese on the selective catalytic hydrogenation of CO_x in the presence of light hydrocarbons over Ni/Al₂O₃: An experimental and computational study

Shadravan, Vahid; Bukas, Vanessa Jane; Gunasooriya, G.T. Kasun Kalhara; Waleson, Jason; Drewery, Matthew ; Karibika, Joel; Jones, Jamie; Kennedy, Eric; Adesina, Adesoji; Nørskov, Jens Kehlet

Total number of authors:

11

Published in:

A C S Catalysis

Link to article, DOI:

[10.1021/acscatal.9b04863](https://doi.org/10.1021/acscatal.9b04863)

Publication date:

2020

Document Version

Publisher's PDF, also known as Version of record

[Link back to DTU Orbit](#)

Citation (APA):

Shadravan, V., Bukas, V. J., Gunasooriya, G. T. K. K., Waleson, J., Drewery, M., Karibika, J., Jones, J., Kennedy, E., Adesina, A., Nørskov, J. K., & Stockenhuber, M. (2020). Effect of manganese on the selective catalytic hydrogenation of CO_x in the presence of light hydrocarbons over Ni/Al₂O₃: An experimental and computational study. *A C S Catalysis*, 10, 1535-1547. <https://doi.org/10.1021/acscatal.9b04863>

General rights

Copyright and moral rights for the publications made accessible in the public portal are retained by the authors and/or other copyright owners and it is a condition of accessing publications that users recognise and abide by the legal requirements associated with these rights.

- Users may download and print one copy of any publication from the public portal for the purpose of private study or research.
- You may not further distribute the material or use it for any profit-making activity or commercial gain
- You may freely distribute the URL identifying the publication in the public portal

If you believe that this document breaches copyright please contact us providing details, and we will remove access to the work immediately and investigate your claim.



This project has received Funding from the European Union's Seventh Framework Programme and Horizon 2020 Research and Innovation Programme under Marie Skłodowska-Curie Actions grant no. 713683 (H2020)



Effect of Manganese on the Selective Catalytic Hydrogenation of CO_x in the Presence of Light Hydrocarbons Over Ni/Al₂O₃: An Experimental and Computational Study

Vahid Shadravan,^{†,||} Vanessa J. Bukas,^{§,||} G. T. Kasun Kalhara Gunasooriya,^{§,||} Jason Waleson,[†] Matthew Drewery,[†] Joel Karibika,[†] Jamie Jones,[†] Eric Kennedy,^{†,||} Adesoji Adesina,[‡] Jens K. Nørskov,[§] and Michael Stockenhuber^{*,†,||}

[†]Chemical Engineering, School of Engineering, The University of Newcastle, Callaghan, NSW 2308, Australia

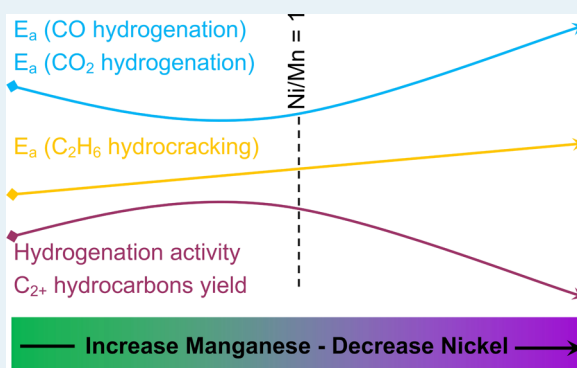
[‡]ATODATECH LLC, Pasadena, California 91101, United States

[§]Catalysis Theory Center, Department of Physics, Technical University of Denmark, DK-2800 Lyngby, Denmark

Supporting Information

ABSTRACT: The promoting effect of manganese on the Ni/Al₂O₃ catalyst for the hydrogenation of carbon oxides, in the presence of light hydrocarbons, was studied. Ni/Al₂O₃ displayed a high activity for the complete conversion of CO and CO₂ to methane and C₂₊ hydrocarbons. Moreover, over a discrete and relatively narrow temperature range, the net concentration of light C₂₊ hydrocarbons was elevated, with the exit stream containing a higher concentration of C₂₊ species than was present in the feed stream and the product stream being virtually free of carbon oxides. It is found that the addition of manganese can enhance the selectivity toward the production of light hydrocarbons. A series of Ni–Mn/Al₂O₃ catalysts, prepared with different Ni/Mn ratios, were studied. Various characterization techniques such as X-ray diffraction (XRD) analysis, CO and H₂ chemisorption, in situ nitric oxide adsorption Fourier transform infrared spectroscopy (NO-FTIR), and temperature-programmed reduction (TPR) were performed to gain an insight into how the addition of Mn to the primary catalyst enhances the yield of light hydrocarbons. The origin of Mn promotion was demonstrated through density functional theory (DFT) calculations, which revealed the favorable Mn substitution at the Ni(211) step edge sites under reducing conditions. The affinity of these Mn species toward oxidation stabilizes the CO dissociation product and thus provides a thermodynamic driving force that promotes C–O bond cleavage compared to the Mn-unmodified catalyst surface.

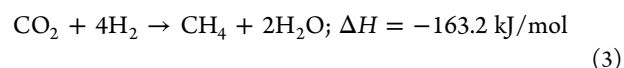
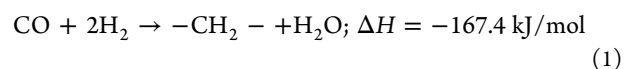
KEYWORDS: CO and CO₂ hydrogenation, bimetallic catalysts, nickel, manganese, density functional theory



INTRODUCTION

For decades, the catalytic hydrogenation of carbon oxides has been widely studied for a wide variety of applications. The worldwide demand for the development of new energy storage devices and resources has reanimated research into CO and CO₂ hydrogenation.¹ Two of the most important and well-known processes for conversion of carbon oxides are Fischer–Tropsch synthesis (FTS)² and carbon oxide methanation.³ FTS is an exothermic polymerization reaction 1, which produces a variety of hydrocarbons, most significantly paraffins, olefins, and alcohols.⁴

The FTS process has received a renewed interest for producing hydrocarbons from both CO and CO₂.⁵ Carbon oxide methanation reactions 2 and 3 have also been used for various applications, such as hydrogen purification for use in ammonia synthesis and fuel cells, producing synthetic natural gas (SNG) and chemical storage of electricity.^{1,6}



Significant quantities of carbon monoxide and carbon dioxide, present as undesirable byproducts, can inhibit commercialization of different processes, especially those involving the catalytic synthesis of hydrocarbons.^{7,8} For these applications, removing CO and CO₂ from a stream containing hydrocarbons is essential. Under these circumstances, it is necessary that carbon oxide hydrogenation does not reduce the initial concentration of C₂₊ hydrocarbons in the feed stream.

Received: November 10, 2019

Revised: December 12, 2019

Published: December 24, 2019

Group VIII transition metals have been extensively studied for carbon oxide hydrogenation and are generally proven to be highly active catalysts. Among this group, nickel has been widely investigated for both FTS and methanation because of its high activity and relatively low cost. However, nickel has not been used as FTS catalyst because of its high selectivity toward methane formation.^{2,9–11} Improving the catalytic properties of nickel-based catalysts for CO_x hydrogenation has been the aim of much research in this area. In these studies, using a second metal as a promoter to form bimetallic nanoparticles, has been established as a technique to enhance the catalytic performance of Ni catalysts. It is found that the structural and electronic properties of single metal particles are significantly changed following the addition of a second metal to form bimetallic nanoparticles. These changes have been shown to engender a notable influence on the performance of the catalyst, in terms of both activity and selectivity.^{11–17}

Manganese has been used to improve both nickel-based and other CO_x hydrogenation catalysts. Differing effects on the catalyst (following the addition of manganese) such as its structural and electronic properties, carbon deposition, and the dispersion of the active sites have been found.^{18–22}

In this work, we present an assessment of the catalytic performance of a series of Ni–Mn/Al₂O₃ catalysts for hydrogenation of CO and CO₂ where the carbon oxides are present in a gas stream together with a significant concentration of light hydrocarbons. The primary focus of this study is to explore the influence of manganese addition to Ni/Al₂O₃ on the activity for a complete conversion of CO_x and selectivity toward enhancing the yield of production for light hydrocarbons and catalyst properties.

METHODS

Catalyst Testing. A series of Ni–Mn/Al₂O₃ catalysts were prepared by the incipient wetness method. The total metal loading for each catalyst was adjusted to 12 wt %.

Table 1 illustrates the labels and calculated metal contents for each sample.

Table 1. Labels and Calculated Metal Contents of Catalysts

catalyst label	Ni (wt %)	Mn (wt %)	Ni/Mn
Ni/Mn 12:0	12.0	0.0	N/A
Ni/Mn 10:2	10.0	2.0	5.0
Ni/Mn 8:4	8.0	4.0	2.0
Ni/Mn 6:6	6.0	6.0	1.0
Ni/Mn 4:8	4.0	8.0	0.5
Ni/Mn 2:10	2.0	10.0	0.2
Ni/Mn 0:12	0.0	12.0	0.0

Hydrated metal nitrates for Ni (Ni(NO₃)₂·6H₂O, Sigma-Aldrich, 99.999%) and Mn (Mn(NO₃)₂·4H₂O, Sigma-Aldrich, 97%) were used as precursors. Alumina spheres (Sasol, Alumina Spheres 1.8/210) were ground and calcined at 500 °C and used as catalyst supports. To prepare each catalyst, a predetermined amount of metal precursors to achieve the desired metal loading and Ni/Mn ratio was dissolved in distilled water. The solution was then added dropwise slowly to the support powder with continuous mixing. The slurry was dried in two steps: initially at 80 °C for 12 h and at 110 °C for 12 h. The dried slurry was then transferred to a furnace for calcination in static air at 500 °C. The catalysts were sieved and particles between 250 and 425 μm were collected. For

each run, 250 mg of the sized catalyst particles and 200 mg of quartz sand were mixed (to avoid formation of any hotspots and dilute the catalyst). A tubular fixed-bed reactor was used to perform the catalytic experiments. Prior to each run, the fresh catalyst was reduced in hydrogen flow at 500 °C for 2 h in situ. Temperature-programmed reaction (TPR) analysis was performed at atmospheric pressure in the range of 150–500 °C.

The feed stream contained CO, CO₂, and H₂ with light alkanes and alkenes (CH₄, C₂H₄, C₂H₆, C₃H₆, and C₃H₈). Four different feed compositions were used to analyze the catalyst performance. The compositions of each feed were adjusted based on the ratio of H₂ to all other reactive components, i.e., CO, CO₂, C₂H₄, C₂H₆, C₃H₆, and C₃H₈. In this case, each feed was labeled as the value of H₂/other ratio (Table 2).

Table 2. Composition of Each Feed Stream

H ₂ /other	partial pressure (kPa)			
	1/1	1.5/1	2/1	4/1
H ₂	9.46	14.2	18.9	37.8
CO	2.03	2.03	2.03	2.03
CO ₂	0.68	0.68	0.68	0.68
CH ₄	8.11	8.11	8.11	8.11
C ₂ H ₄	0.34	0.34	0.34	0.34
C ₂ H ₆	0.34	0.34	0.34	0.34
C ₃ H ₆	0.03	0.03	0.03	0.03
C ₃ H ₈	0.03	0.03	0.03	0.03
He	80.3	75.6	70.9	52.0
total	101	101	101	101

Conversion (*X*), selectivity (*S*), and product yield (*Y*) are defined by equations 4–6. The conversion was calculated for CO and CO₂. The selectivity and yield were calculated for light hydrocarbons (C₂–C₄). It should be noted that the selectivity and yield were calculated based on the total mole number of carbon in C₂₊ hydrocarbons. Experiments for CO and CO₂ hydrogenation in the absence of hydrocarbons in the feed stream were performed. It is found that from CO₂ hydrogenation under this condition, the major product is methane and the concentration of higher hydrocarbons was negligible. Therefore, the selectivity and yield of C₂–C₄ hydrocarbons was calculated based on CO conversion.

The specific reaction rate and activation energy value were determined for Ni–Mn/Al₂O₃ catalysts under differential reaction conditions (below 10% conversion). In this case, the reaction of hydrogen with CO, CO₂, and C₂H₆ has been analyzed separately. The activation energy values were calculated using the Arrhenius equation²³

$$X_{\text{CO or CO}_2} = \frac{n_{\text{CO or CO}_2, \text{in}} - n_{\text{CO or CO}_2, \text{out}}}{n_{\text{CO or CO}_2, \text{in}}} \times 100 \quad (4)$$

$$S_{\text{C}_2-\text{C}_4} = \frac{n_{\text{C}_2-\text{C}_4, \text{out}} - n_{\text{C}_2-\text{C}_4, \text{in}}}{n_{\text{CO, in}} - n_{\text{CO, out}}} \times 100 \quad (5)$$

$$Y_{\text{C}_2-\text{C}_4} = \frac{n_{\text{C}_2-\text{C}_4, \text{out}} - n_{\text{C}_2-\text{C}_4, \text{in}}}{n_{\text{CO, in}}} \times 100 \quad (6)$$

Inductively Coupled Plasma-Optical Emission Spectroscopy (ICP-OES). The elemental composition of the catalysts for Ni and Mn was determined by an ICP-OES

spectrometer (Varian Radial 715-ES). The sample preparation consisted of digestion and dilution steps. Microwave-assisted digestion of each sample occurred in a mixture of HNO₃, HCl, and HBF₄ as solvent.²⁴ The solutions were then diluted to a suitable extent and analyzed by the spectrometer.

X-ray Diffraction (XRD) Analysis. A Philips X'Pert MPD with copper anode ($K\alpha = 1.54060 \text{ \AA}$ at 40 kV and 40 mA) was used to obtain powder XRD patterns for crystal-phase investigation. Obtained data were analyzed using X'Pert Highscore Plus²⁵ and Match²⁶ programs. The reference patterns were downloaded from inorganic crystal structure database (ICSD) and crystallography open database (COD) and compared to the experimental patterns for each sample.

Temperature-Programmed Reduction (TPR). TPR analysis was performed in a purpose-built apparatus with a mixture of H₂ (2%) and Ar (98%). Prior to each run, fresh samples were thermally treated at 400 °C for 30 min. For the TPR experiments, a temperature ramp of 10 °C/min was imposed on the catalyst sample and the flow rate for each sample/reference lines was fixed at 50 mL/min. The moles of hydrogen consumed was analyzed with a thermal conductivity detector (TCD). A similar mass of sample (225 mg) was used for each analysis, so no normalization was needed during postrun analysis.

Nitric Oxide Adsorption Fourier Transform Infrared (NO-FTIR) Spectroscopy. Nitric oxide adsorption in situ experiments were carried out in an ultrahigh-vacuum cell. Spectra during all key steps (activation/reduction, adsorption, and desorption) were recorded using a Bruker Tensor27 FTIR spectrometer. Wafers ($\approx 15 \text{ mg}$) were pressed using 13 mm dies. The wafers were heated up to 500 °C at a rate of 5 °C/min and maintained at that temperature for 30 min under vacuum. The sample was then reduced in situ at 500 °C by injecting 10 mbar H₂ into the cell and remaining at these conditions for 10 min followed by evacuation of the cell (and catalyst) for 10 min. The reduction procedure consisted of three cycles of this H₂ injection/evacuation procedure. The nitric oxide adsorption spectra were collected at 50 °C at pressures ranging from 1.0×10^{-4} mbar to 10 mbar. After completion of the adsorption step, the samples were heated to 500 °C with 5 °C/min and spectra were collected to study desorption of NO from the samples. For adsorption/desorption difference spectra, the spectrum of a "clean", activated, and reduced catalyst sample at 50 °C was subtracted. The gas-phase NO spectrum was also recorded in the empty cell to confirm the absence of gas-phase contaminants.

H₂ and CO Chemisorption. A volumetric chemisorption apparatus was used to quantitatively determine the capacity of each catalyst for H₂ and CO chemisorption. The reactor/sample tube used for chemisorption experiments was a U-shaped quartz tube with 10 mm OD. Prior to each experiment, the samples were calcined in 100 cm³/min air at 500 °C for 2 h and purged in He for 30 min followed by reduction in 100 cm³/min H₂ at 500 °C for 2 h. For each sample, 250 mg of catalyst was calcined and reduced (in situ) in the apparatus for chemisorption analysis. The apparatus and samples were outgassed at 1.0×10^{-4} mbar using foreground and turbo pumps prior to each experiment. Hydrogen and carbon monoxide chemisorptions were performed separately at 40 °C over a pressure range of 30–90 mbar. Based on the volume of chemisorbed H₂ and CO, the metal particle dispersion (*D*), specific surface area (*SA*), and average particle size (*d*) were calculated using eqs 7–9²⁷

$$D (\%) = \frac{S_f \times n_{\text{gas}} [\text{mol}] \times F_w [\text{g/mol}]}{\text{wt } \% \times W_{\text{sample}} [\text{g}]} \times 100 \quad (7)$$

$$SA (\text{m}^2/\text{g}) = \frac{S_f \times n_{\text{gas}} [\text{mol}] \times \sigma_m [\text{m}^2/\text{atom}] \times N_A [\text{atom/mol}]}{\text{wt } \% \times W_{\text{sample}} [\text{g}]} \quad (8)$$

$$d (\text{nm}) = \frac{6000}{S [\text{m}^2/\text{g}] \times \rho_m [\text{g}/\text{cm}^3]} \quad (9)$$

where n_{gas} is the number of moles of gas adsorbed on the metal particles, F_w is the formula weight of the particle, S_f is the stoichiometric factor, wt % is the weight percent of the metal particle in the sample, W_{sample} is the total weight of the sample, σ_m is the atomic cross-sectional area of metal, N_A is the Avogadro number, and ρ_m is the metal particle density.

Density Functional Theory (DFT) Calculations. Periodic spin-polarized DFT calculations were performed using the RPBE functional,²⁸ a plane-wave basis set with a cutoff kinetic energy of 400 eV, and the projector-augmented wave method,²⁹ as implemented in the Vienna ab initio simulation package (VASP).^{30,31} When explicitly stated, a Hubbard *U* correction of 3.9 eV was applied for all Mn atoms.³² Ni terrace sites were modeled using a three-layer Ni(111) $p(3 \times 3)$ unit cell, and Ni step sites were modeled using a three-layer Ni(211) $p(3 \times 1)$ unit cell, while the corresponding Brillouin zones were sampled with a $(3 \times 3 \times 1)$ Monkhorst–Pack grid.³³ To model MnO stripes, a three-layer Ni(111) $p(4 \times 2)$ unit cell was used and the Brillouin zone was sampled with a $(1 \times 4 \times 1)$ Monkhorst–Pack grid. In all of the slabs, the bottom two layers were constrained at the bulk positions, while the top layer and the adsorbed species were fully relaxed. The slabs were separated in the perpendicular *z*-direction by 15 Å of vacuum, and a dipole correction was applied. The electronic convergence criterion was 10^{-5} eV, while the force criterion for geometry relaxation was 0.05 eV \AA^{-1} for all forces.

To determine the relative stability of different configurations that substitute Mn for Ni atoms in Figure 1, the chemical potential per Mn atom (μ^{Mn}) was calculated as

$$\mu^{\text{Mn}} = (E^{\text{Ni}_{\text{slab}} \cdot n \text{Mn}^{\text{sub}}(\text{OH})_x} + nE^{\text{Ni}_{\text{fcc}}} - E^{\text{Ni}_{\text{slab}}} - nE^{\text{Mn}} - x\mu^{\text{H}_2\text{O}} + 1/2x\mu^{\text{H}_2})/n \quad (10)$$

where *E* denotes the calculated DFT energies and *n* corresponds to the number of Mn atoms in the corresponding structure. In our calculations, Ni and Mn are referenced to bulk face-centered cubic (fcc) Ni and bulk metallic Mn, respectively. The hydrogen and oxygen chemical potentials (μ^{H} and μ^{O}) are referenced to gas-phase H₂ and H₂O ($1/2\mu^{\text{H}_2}$ and $\mu^{\text{H}_2\text{O}} - \mu^{\text{H}_2}$). Using a similar approach, the relative stability of Mn_{*n*}O_{*x*}H_{*y*} stripes on a Ni slab was calculated as

$$\mu^{\text{Mn}} = (E^{\text{Ni}_{\text{slab}} \cdot \text{Mn}_n \text{O}_x \text{H}_y} - E^{\text{Ni}_{\text{slab}}} - nE^{\text{Mn}} - x\mu^{\text{H}_2\text{O}} + x\mu^{\text{H}_2} - 1/2y\mu^{\text{H}_2})/n \quad (11)$$

Chemical potentials of gas-phase species were calculated by augmenting the corresponding DFT energies (*E*) with contributions for zero-point energy (ZPE), entropy (*S*), and pressure (*P*)

$$\mu = E + \text{ZPE} - \text{TS} + \text{RT} \ln P \quad (12)$$

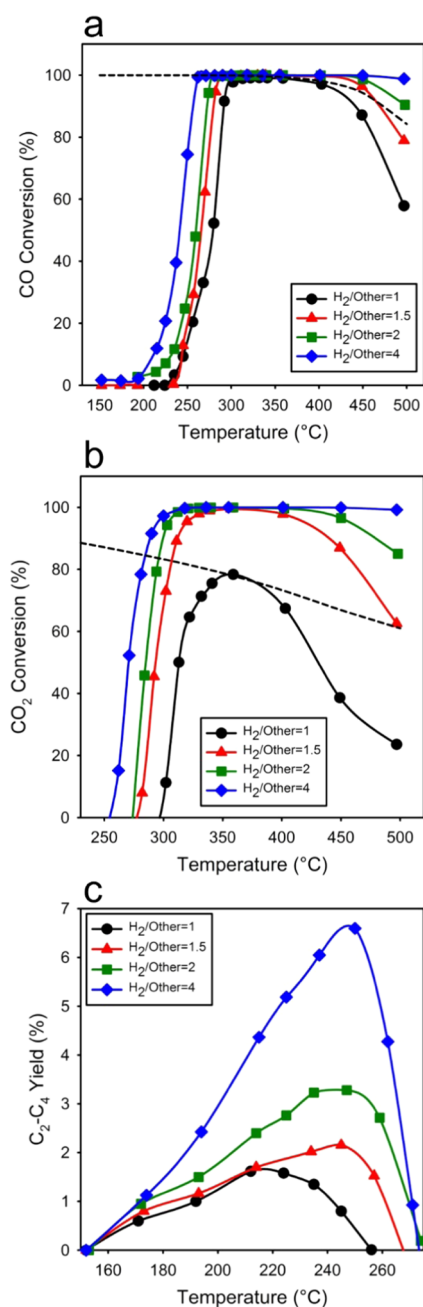


Figure 1. (a) CO conversion, (b) CO₂ conversion, and (c) yield of production of C₂–C₄ hydrocarbons for different feed compositions over Ni/Al₂O₃ (Ni/Mn 12:0) catalyst.

The latter terms were calculated from DFT based on a normal-mode analysis and using the experimental values for operating temperature (~ 260 °C) and pressures ($P_{\text{H}_2} = \sim 0.5$ bar, $P_{\text{CO}} = \sim 0.02$ bar). Finally, we included a ZPE term associated with the presence of an adsorbate, while changes in surface entropy due to adsorption were considered to be small and thus neglected.

RESULTS AND DISCUSSION

Catalyst Testing. The temperature-programmed catalyst experiments were conducted at atmospheric pressure over the temperature range of 150–500 °C. Initially, Ni/Al₂O₃ catalysts were examined, with different feed compositions as outlined in Table 2. The primary reason for this aspect of the research was

to study the effect of excess H₂ on catalyst activity (in the case of higher conversion of CO and CO₂ at lower temperatures) and the selectivity toward the production of light hydrocarbons (C₂₊). The changes in the level of conversion (for CO and CO₂) with temperature for different feed compositions over the Ni/Al₂O₃ catalyst are shown in Figure 1. The conversion of carbon monoxide and carbon dioxide was first detected at different temperatures for all experiments. Carbon monoxide conversion commenced and reached its maximum conversion level over a temperature range which was significantly lower than that of CO₂. Others have also reported that during cohydrogenation of CO and CO₂, the conversion of CO commences at a lower temperature than CO₂ hydrogenation.^{34–36} At higher temperatures, conversion of both CO and CO₂ decreased with increasing temperature. One explanation for this observation is both CO and CO₂ hydrogenation reactions are highly exothermic and increasing temperature results in reducing the net level of conversion.⁶ Thermodynamic and chemical equilibrium calculations were performed to discuss and explain the optima in Figure 1, especially for the feed stream with a H₂/other ratio = 1. Based on the thermodynamic equilibrium calculations, the optima in both CO and CO₂ conversion can be explained by the presence of thermodynamic limits. It is also clear from these data that increasing the amount of excess hydrogen enhances the activity of CO and CO₂ hydrogenation. Increasing the H₂ ratio from 1 to 4 resulted in decrease in temperature of approximately 40 °C for maximum CO and CO₂ conversion.

The main product of CO and CO₂ hydrogenation over nickel catalysts is methane. However, the formation of light hydrocarbons also was observed, and the yield of these hydrocarbons, for each feed composition studied, is shown in Figure 1. The formation of C₂₊ hydrocarbons commences at low temperatures coinciding with the temperature at which CO conversion is detected. The yield of C₂₊ hydrocarbons then reached a maximum for each run and subsequently decreased with increasing temperature. With continuing increase in reaction temperature, the light hydrocarbons in the feed stream were converted, mainly to methane. Additional hydrogen in the feed stream enhanced the C₂₊ production yield, and the feed with the highest concentration of hydrogen resulted in the highest yield of C₂₊ hydrocarbons. Moreover, the starting temperature for C₂₊ consumption increased by approximately 10 °C for a hydrogen ratio of 4:1 compared to 1:1.

To analyze the performance of catalysts with different Ni/Mn ratios, experiments were performed with feed composition with the highest activity or level of CO_x conversion and the highest yield of C₂–C₄ hydrocarbons. The results disclose that the starting temperature for both CO and CO₂ conversion is dependent on the Ni/Mn ratio of the catalysts examined (Figure 2). For instance, the Ni/Mn ratios of 5 and 2 increased the activity for CO and CO₂ conversion compared to the single metallic Ni/Al₂O₃ benchmark catalyst. By decreasing the Ni/Mn ratio below 2, it is found that the activity was significantly reduced as the manganese content increased. The single metallic Mn/Al₂O₃ catalyst did not show any activity for CO conversion. It is found that above 300 °C, carbon dioxide conversion was detected and CO production was observed over the same temperature range. This is most probably due to dry reforming of methane (DRM) or reverse water–gas shift (RWGS) reactions. The activity of manganese-containing

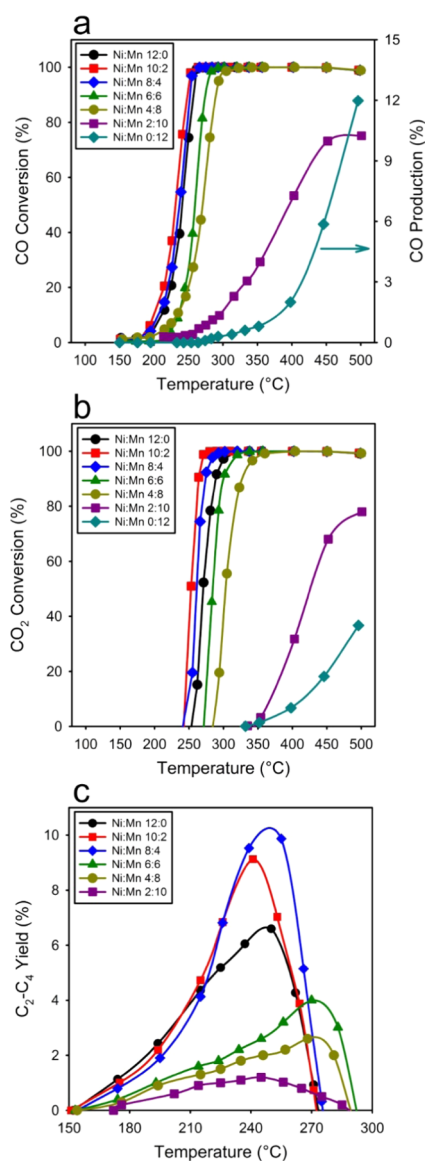


Figure 2. (a) CO conversion, (b) CO₂ conversion, and (c) yield of production of C₂–C₄ hydrocarbons for catalysts with varying Ni/Mn ratios in the feed stream with H₂/other = 4 feed composition.

catalysts for both DRM and RWGS has been reported by other researchers.^{37,38}

The yield of light hydrocarbons also changed and is dependent on the nickel and manganese concentrations in the catalysts (Figure 2). Similar to CO and CO₂ conversion, the catalysts with Ni/Mn ratios of 5 and 2 showed elevated levels of C₂–C₄ yield compared to Ni/Al₂O₃ catalysts. Conversely, the yield of C₂–C₄ decreased for catalysts with Ni/Mn ratio lower than 2.

From a process perspective, the existence of a temperature window (approximately between 240 and 280 °C), in which CO and CO₂ conversion is essentially complete (100%) and the C₂–C₄ hydrocarbons concentration is elevated when compared to that in the feed stream, is intriguing. By increasing the reaction temperature above that temperature window, light hydrocarbons are consumed. The increase of methane concentration at higher temperature suggests that cracking of light hydrocarbons to form methane is taking place.

To further understand the influence of manganese addition, estimates for the activation energy value for the reaction of CO, CO₂, and C₂H₆ with hydrogen over Ni/Al₂O₃ and Ni–Mn/Al₂O₃ (with Ni/Mn = 2 and 0.5) catalysts was obtained. In this study, the activation energy values were calculated from the specific reaction rates in differential regime using the Arrhenius equation. The calculated values are summarized in Table 3.

Table 3. Calculated Activation Energy Values for the Reaction of CO, CO₂, and C₂H₆ with H₂ Over Ni/Mn 12:0, Ni/Mn 8:4, and Ni/Mn 4:8 Catalysts

catalyst	reactant	activation energy value (kJ/mol)
Ni/Mn 12:0	CO	98.3
Ni/Mn 8:4	CO	93.3
Ni/Mn 4:8	CO	113
Ni/Mn 12:0	CO ₂	80.3
Ni/Mn 8:4	CO ₂	75.7
Ni/Mn 4:8	CO ₂	99.4
Ni/Mn 12:0	C ₂ H ₆	151
Ni/Mn 8:4	C ₂ H ₆	161
Ni/Mn 4:8	C ₂ H ₆	169

For CO hydrogenation, the activation energy values followed the order of Ni/Mn 4:8 > Ni/Mn 12:0 > Ni/Mn 8:4. The calculated values of this study are in good agreement with the activation energy values reported for CO hydrogenation over nickel-based catalysts (approximately between 80 and 120 kJ/mol).^{39–43}

It is found that by adding a moderate loading of manganese (Ni/Mn, 8:4) to the Ni/Al₂O₃ catalyst, the activation barrier for CO hydrogenation slightly decreased. However, adding more quantities of manganese (Ni/Mn, 4:8) resulted in an increase in the activation energy value.

The CO₂ hydrogenation activation energy value followed the same order as CO hydrogenation over different catalysts (Ni/Mn 4:8 > Ni/Mn 12:0 > Ni/Mn 8:4). Similar to CO hydrogenation, the activation energy value for CO₂ hydrogenation decreased by adding a moderate amount of manganese (Ni/Mn = 2) to Ni/Al₂O₃ and increased by further increasing of the added manganese (Ni/Mn = 0.5). The values calculated in this study are also close to the reported activation energy value of CO₂ hydrogenation over nickel catalysts.^{40,43,44}

The calculated values for ethane hydrocracking in this study are of the same order of magnitude compared to the reported values in the literature.^{45–47} It is found that the activation barrier for ethane hydrocracking increased by adding manganese to the primary Ni/Al₂O₃ catalyst. In this case, the activation energy value for ethane hydrocracking can be arranged in the following order: Ni/Mn 4:8 > Ni/Mn 8:4 > Ni/Mn 12:0.

Differences in the activity and selectivity for bimetallic catalysts have been explained in a number of ways, such as changes in the number of active metal sites and the formation of catalytically active sites with new characteristics,⁴⁸ which are discussed in the following sections.

ICP-OES. Table 4 shows the elemental analysis (Ni and Mn) obtained for each catalyst by the ICP-OES technique. The results are reasonably close to the amount of nickel and manganese initially impregnated. The ratio of Ni/Mn is similar

Table 4. Metal Contents of Each Catalyst Based on ICP-OES Analysis

catalyst	Ni (wt %)	Mn (wt %)	Ni/Mn
Ni/Mn 12:0	11.6	0.0	N/A
Ni/Mn 10:2	9.5	1.9	5.0
Ni/Mn 8:4	7.7	3.8	2.0
Ni/Mn 6:6	5.7	5.8	1.0
Ni/Mn 4:8	3.8	7.8	0.5
Ni/Mn 2:10	2.3	9.5	0.2
Ni/Mn 0:12	0.0	11.5	0.0

to the values invoked during catalyst preparation via incipient wetness.

XRD. The X-ray powder diffraction patterns of calcined samples were collected for crystal and structural analysis of the catalysts (Figure 3). The following reflections were detected on

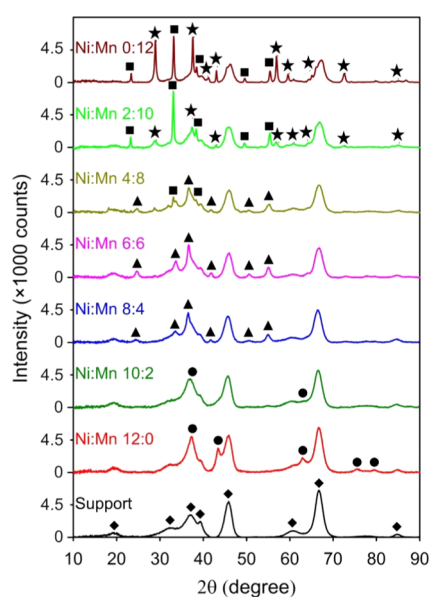


Figure 3. XRD patterns for the alumina support and all catalysts. The symbols \blacklozenge , \bullet , \blacktriangle , \blacksquare , and \star were used to mark the identified reflections for Al_2O_3 , NiO , NiMnO_3 , Mn_2O_3 , and MnO_2 phases, respectively.

the alumina support: 19, 32, 37, 39, 61, 67, and 85° .⁴⁹ It is found that the single-metal $\text{Ni}/\text{Al}_2\text{O}_3$ catalyst contains NiO and NiAl_2O_4 particles, and most notably the distinct NiO reflections were observed at 37, 43, 63, 76, and 80° .⁵⁰ For NiAl_2O_4 , reflections at 37, 45, 59, and 66° have been reported.⁵¹ However, these reflections were masked by the reflections of other materials such as Al_2O_3 , NiO , and NiMnO_3 , which have higher intensities. It is clear that the intensity of the reflection at approximately 64° decreased as a result of a lower concentration of NiAl_2O_4 in samples that have lower nickel content (especially for single-metal $\text{Mn}/\text{Al}_2\text{O}_3$).

By increasing the manganese content in the samples, NiO reflections also became less intensive and new reflections were observed. For samples with Ni/Mn ratios of 2 (Ni/Mn 8:4), 1 (Ni/Mn 6:6), and 0.5 (Ni/Mn 4:8), reflections corresponding to NiMnO_3 phase emerged. The reflections attributed to NiMnO_3 are at 24, 34, 37, 42, 50, and 56° .⁵² The formation of NiMnO_3 particles on bimetallic $\text{Ni}-\text{Mn}/\text{Al}_2\text{O}_3$ catalyst has been reported previously.⁵³ Two oxide forms of manganese were also found for the samples with higher manganese

contents (Ni/Mn 4:8, Ni/Mn 2:10, and Ni/Mn 0:12). The presence of Mn_2O_3 was identified with two low-intensity reflections at 33 and 38° for the catalyst with a Ni/Mn ratio of 0.5. For the other two samples with higher Mn content, the reflections at 23, 33, 38, 51, and 55° were identified as Mn_2O_3 .⁵⁴ Manganese(IV) oxide (MnO_2) was observed for the sample with a Ni/Mn ratio of 0.2 and the single-metal $\text{Mn}/\text{Al}_2\text{O}_3$. The reflections at 29, 38, 41, 43, 57, 60, 64, 73, and 86° correspond to MnO_2 particles on the samples.⁵⁵

TPR. The reducibility of metal sites for catalysts was investigated by temperature-programmed reduction. Figure 4

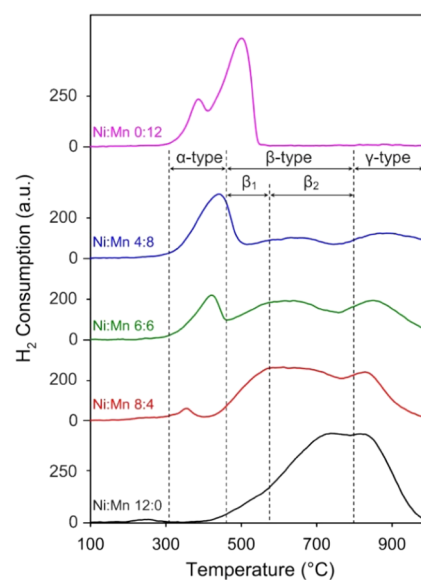
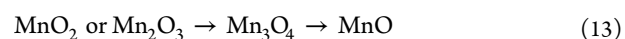


Figure 4. Temperature-programmed reduction profiles or samples with different Ni and Mn contents.

presents the TPR profiles for single-metal $\text{Ni}/\text{Al}_2\text{O}_3$ and $\text{Mn}/\text{Al}_2\text{O}_3$, together with bimetallic $\text{Ni}-\text{Mn}/\text{Al}_2\text{O}_3$ samples having Ni/Mn ratios of 2, 1, and 0.5. The consumption of hydrogen commenced at temperature above 300°C for all of the samples. In general, the reducible nickel species on alumina-supported catalysts are classified into four types: α , β_1 , β_2 , and γ .^{56–58} The α -type NiO (also known as free NiO weakly bonded to alumina) species are usually reducible in low-temperature regions. The midrange or β -type NiO species interact more strongly with the support and are reduced at a higher temperature range than α -type NiO . The β -type nickel oxide is classified into two subgroups: β_1 -type and β_2 -type. The β_1 -type and β_2 -type are known as Ni-rich and Al-rich mixed oxide phases, respectively. In this case, the Ni-rich phase is more reducible than the Al-rich phase. The Ni-containing species reduced in the high temperature range is γ -type NiO . It is reported that the γ -type NiO is the stable nickel aluminate (NiAl_2O_4).^{59,60}

The TPR profile for the single-metal $\text{Mn}/\text{Al}_2\text{O}_3$ sample shows peaks in the $300\text{--}500^\circ\text{C}$ range. It is reported that alumina-supported manganese oxides are usually reduced via a two-step reduction process (13)^{53,61–63}



For bimetallic $\text{Ni}-\text{Mn}$ catalysts, the TPR profiles changed significantly with varying Ni/Mn ratio. It is found that by decreasing the Ni/Mn ratio, detection of hydrogen consumption shifted to lower temperatures. There is no distinct

peak attributable to manganese oxide reduction for all of the Ni–Mn/Al₂O₃ samples examined with TPR, which is consistent with the XRD results of these samples. The TPR profiles for bimetallic Ni–Mn/Al₂O₃ catalysts showed that the concentration of Ni-containing species in the β and γ regions decreased following the addition of additional manganese to the catalysts. Moreover, a new peak emerged, located at more reducible α -type region in the TPR spectra. The presence of more reducible Ni-containing species for Ni–Mn/Al₂O₃ samples can be attributed to the formation of the NiMnO₃ complex. These observations from the TPR analysis of the Ni–Mn/Al₂O₃ catalysts are in good agreement with the results reported in the literature.^{20,22,53}

NO-FTIR Spectroscopy. To understand the catalytic properties of the samples with different nickel and manganese contents, samples were analyzed by in situ infrared spectroscopy using nitric oxide as a probe molecule (NO-FTIR spectroscopy). Characteristic information of the catalysts can be investigated by the NO-FTIR technique.^{11,12,64} The coordinated nitric oxide molecules, bonded to the catalyst's active sites, have properties similar to those of carbon monoxide on the active sites.⁶⁵ This makes the NO-FTIR technique even more suitable for analysis of the catalysts for processes such as CO_x hydrogenation and involving CO activation. Nitric oxide FTIR analysis was performed on Ni/Al₂O₃, Mn/Al₂O₃, and bimetallic Ni–Mn/Al₂O₃ with Ni/Mn ratios of 2, 1, and 0.5. All of the samples displayed different catalytic performances for hydrogenation of CO_x in the presence of light hydrocarbons. The results of the catalyst screening experiments showed that addition of manganese changed the activity of Ni/Al₂O₃ for conversion of CO and CO₂. Moreover, the yield of production for C₂–C₄ hydrocarbons was also varied by changing the Ni/Mn ratio.

Following the adsorption of NO, several peaks arose at different wavenumbers in the catalyst spectra. These surface species are generally divided into two main categories as reactive and nonreactive NO adsorption surface species. The reactive adsorption (depending on the adsorptive sample and adsorption conditions) occurs when nitric oxide acts as a reducing/oxidizing agent or disproportionates. Compounds such as NO⁺, NO_x[–] ($x = 2, 3$), N₂O, and NO₂ can be formed during the reactive adsorption of NO. On the other hand, NO surface species such as mononitrosyl and dinitrosyl complexes are the products of nitric oxide nonreactive adsorption.⁶⁵ In the current investigation, the focus is on the nonreactive NO adsorption.

Figures S1–S6 (Supporting Information) demonstrate the NO-FTIR spectra for the samples studied. Sections “a” and “b” show the adsorption and desorption spectra, respectively. For the samples that contained nonreactive NO adsorption, zoomed-in windows representing the region for mononitrosyl adsorption are highlighted. The peaks present in the spectra at around 1850 cm^{–1} wavenumbers (below the gaseous NO frequency) can be assigned as mononitrosyls arising from the nonreactive adsorption of NO on the Ni-containing samples.^{66–69} The disappearance of these peaks following the evacuation of the FTIR cell also confirms the assignment of the weakly bound peak at 1850 cm^{–1}. It should be noted that, compared to mononitrosyls, the formation of dinitrosyls is less likely at low NO coverage.^{70,71} Other peaks appearing at wavenumbers around 1300 and 1600 cm^{–1} can arise as a result of the reactive adsorption of NO molecules on the sample. The peaks are most likely due to the formation of charged and

neutral N_xO_y species such as NO₂ and NO₂[–] surface compounds.^{65,72} These peaks were significantly increased in size by introducing more NO to the sample. In addition, applying a higher temperature was required to desorb these species. Peaks attributable to nonreactive NO adsorption were absent on single-metal Mn/Al₂O₃ samples. It is found that at high levels of NO coverage, the bands assigned as metal–mononitrosyl species are shifted slightly to higher wavenumbers. The explanation for this slight shift is attributed to changes in the oxidation state of the metal to higher values. It is reported that on metals at their highest oxidation state, the formation of linear-type NO is more likely than the bent-type.^{73,74}

The focus of the current study is on the species formed during the nonreactive adsorption of NO, especially metal–mononitrosyls. The nitric oxide molecule has three electron pairs and one unpaired electron in its bonding and antibonding orbitals, respectively. Thus, the bond order of N–O is 2.5 with stretching vibration at a frequency of 1876 cm^{–1} in the gas phase.⁷⁵ Nitric oxide can act as an electron donor (weak Lewis base) and electron acceptor (weak Lewis acid). Therefore, the coordination of NO molecule by partial charge transfer from weakly antibonding (5σ) orbital to a metal site via nitrogen atom forms is possible. In contrast, partial charge transfer from the metal site to nitric oxide molecule or π -back bonding may occur. These partial charge transfers are known as NO molecule coordination and are denoted as NO ^{δ^+} or NO ^{δ^-} . For simplicity, the partial charge symbol (δ) has been removed in many publications.⁶⁵

The metal–mononitrosyl compounds are often formed during the adsorption of NO on transition metals. The formation of these species is the result of a partial charge transfer between the active sites and the NO molecule, which leads to the coordination of NO by NO ^{δ^+} or NO ^{δ^-} . Nitric oxide, in the form NO ^{δ^+} coordination, is basically an electron donor to an electron-accepting site. In contrast, NO, in the form of NO ^{δ^-} coordination, accepts an electron from an electron donor site. The linear and bent geometries of coordinated nitric oxide molecule are the results of NO ^{δ^+} and NO ^{δ^-} , respectively.⁷⁶

To compare the ratio of linear/bent metal–mononitrosyl species on samples with different Ni and Mn contents, the peaks assigned as mononitrosyls were deconvoluted. In this case, adsorption spectra, collected at same NO pressure (2.0×10^{-4} mbar), were chosen. Figure 5 displays the deconvoluted peaks for the nickel-containing samples. The bonding of N–O in bent-type NO is weaker than that in linear-type NO, and its stretching band appears at lower wavenumber. Therefore, in all spectra of Figure 5, the peak with lower wavenumber is the bent and the other peak is linear-type NO.

Figure 6 shows the changes of linear/bent ratio of metal–mononitrosyl compounds on the samples. Comparing this ratio gives an insight into the influence of adding different levels of manganese to Ni/Al₂O₃ catalyst on the electronic properties of catalyst. In fact, the linear/bent ratio represents the ratio of electron-accepting to electron-donating sites on each catalyst.¹² According to Figure 6, decreasing the Ni/Mn ratio resulted in reducing the value of linear/bent ratio. However, for samples with Ni/Mn ratios of 2 and 1, the number of sites reliable for the formation of linear and bent metal–mononitrosyl compounds increased.

The NO-FTIR analysis showed the presence of sites with different electronic properties structure that are responsible for

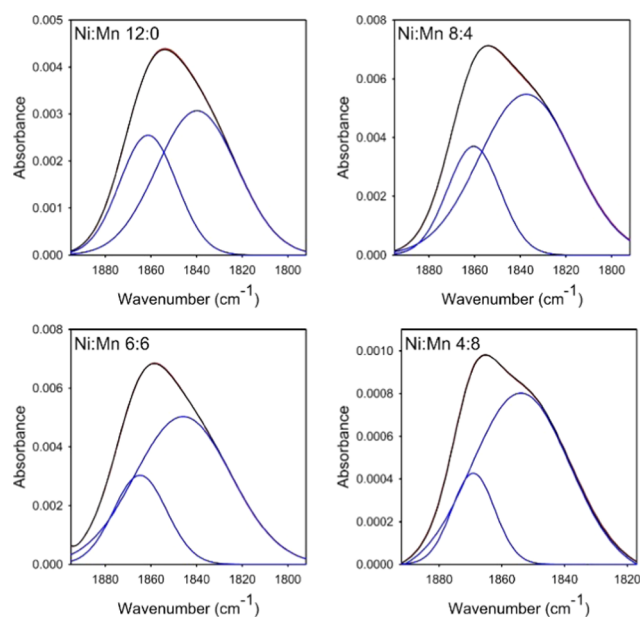


Figure 5. Peak deconvolution for metal–mononitrosyl species formed on nickel-containing samples during in situ NO-FTIR analysis.

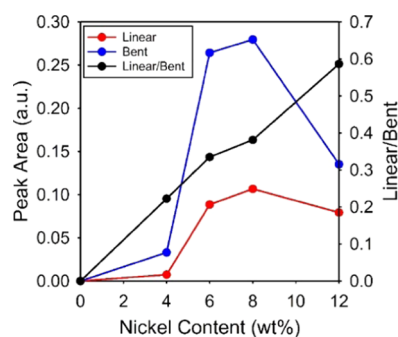


Figure 6. Calculated value of linear/bent ratio of metal–mononitrosyl compounds for catalysts with different Ni/Mn ratios.

linear and bent adsorption configurations of NO. These electron-accepting (linear NO) and electron-donating (bent NO) sites can be interpreted as carbon-accepting and oxygen-accepting sites.^{18,65} It is found that adding manganese to Ni/Al₂O₃ resulted in changing the ratio of linear/bent sites (i.e., C-accepting/O-accepting). Therefore, the enhancement of CO hydrogenation activity and C₂₊ hydrocarbons selectivity by adding manganese to Ni/Al₂O₃ can be explained by decreasing the C-accepting/O-accepting ratio. In this case, the presence of more O-accepting sites in the vicinity of C-accepting sites can decrease the energy barrier for C–O bond cleavage and CO hydrogenation, which is also confirmed by DFT calculations.

The addition of manganese also affected the hydrocracking activity (e.g., ethane hydrocracking). It is reported that the hydrocracking activity over nickel catalysts depends on the C–C bond rupture.^{45,47} In this case, the C–C bond cleavage happens more readily on catalysts with stronger carbon–metal bonding or more carbon-accepting sites.⁴⁶ In this paper, it is found that adding manganese to Ni/Al₂O₃ decreased the ratio of C-accepting/O-accepting sites. These changes resulted in the increasing of the energy barrier for C₂H₆ hydrocracking and C–C bond rupture. This discussion can be used for further explanation of the enhanced selectivity toward higher

hydrocarbons production over some of the Ni–Mn/Al₂O₃ (e.g., Ni/Mn = 2) catalysts compared to the Ni/Al₂O₃ catalyst.

H₂ and CO Chemisorption. To investigate the influence of differing nickel and manganese content on the catalyst properties, the quantity of chemisorbed gas, mole ratio of chemisorbed CO to hydrogen, dispersion, specific surface area, and particle size were estimated. It was found that when reducing the Ni/Mn ratio, the amount of chemisorbed gas (both CO and H₂) decreased (Figure 7). The chemisorption

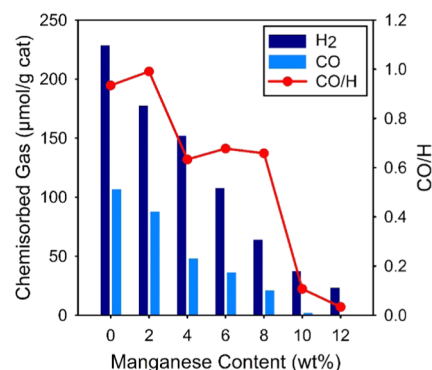


Figure 7. Chemisorbed carbon monoxide, hydrogen, and CO/H ratio on each catalyst.

of CO decreased significantly for catalysts with elevated manganese content. In this case, the amount of CO chemisorbed on single-metal Mn/Al₂O₃ was negligible. On the other hand, H₂ chemisorption occurred on all samples. The dispersion, specific surface area, and particle size were calculated for all samples based on the H₂ consumption (Table 5).

Table 5. Dispersion, Specific Surface Area, and Particle Size Calculated for Metal Particles Based on H₂ Chemisorption

catalyst	<i>D</i> (%)	SA (m ² /g)	<i>d</i> (nm)
Ni/Mn 12:0	23.1	165.3	4.1
Ni/Mn 10:2	18.1	134.3	5.2
Ni/Mn 8:4	15.2	117.0	6.1
Ni/Mn 6:6	10.6	85.3	8.6
Ni/Mn 4:8	6.2	51.6	14.7
Ni/Mn 2:10	3.5	30.2	25.8
Ni/Mn 0:12	2.2	20.0	40.5

The data presented in Table 5 suggest that when decreasing the Ni content in samples, the dispersion and specific area decreased. In contrast, the average particle size increased with decreasing Ni/Mn ratio. Changing the metallic composition of samples showed more influence on the samples with Ni/Mn ratio below 1. For example, the average particle size increased about 4 nm for Ni/Mn = 1 compared to single-metal Ni/Al₂O₃, but the particle size increment is almost 36 nm for Ni/Mn = 0.

For analyzing the parameters achieved from the chemisorption experiments, Ni content (Ni/Mn ratio) versus SA, *D*, and *d* were plotted. The plotted data were analyzed using one of the most commonly used equilibrium models, namely, the Langmuir curve, which is based on monolayer coverage prediction of the adsorbate. This model also suggests that there is no lateral interaction between the sorbed molecules.

The apparent hyperbolic dependency of both dispersion (D) and surface area (SA) with respect to the Ni/Mn ratio implicates “Langmuirian root” of these properties. A reasonable empirical model for the data would be (eqs 14 and 15)

$$y = y_0 + \frac{ax}{b + x} \quad (14)$$

or

$$y = y_0 + \frac{k_1x}{1 + k_2x} \quad (15)$$

where $k_1 = a/b$ and $k_2 = 1/b$, y_0 is the value of the property at Ni/Mn = 0 (no Ni in the catalyst), while k_1 is the property growth rate with respect to Ni content and k_2 is the interaction factor (or binding coefficient) for Ni–Mn during the property evolution. The nonlinear regression for both dispersion and surface area indicates an excellent model fit.

For metal particle diameter (d), the appropriate model is an exponential decay law implicating a pseudo-first-order decay or loss in metal particle size (eq 16). This would suggest that Mn addition increased the propensity for Ni atom agglomeration or aggregation

$$y = c e^{-dx} \quad (16)$$

where c is the particle diameter in the absence of Ni (i.e., Mn crystallite only) and b is the Mn crystallite size loss rate with Ni content. Here, the nonlinear regression also indicates a good model fit.

By comparing the XRD patterns and H₂ chemisorption data, it was found that adding low or medium amounts of manganese (Ni/Mn > 1) led to the formation of moderately dispersed and relatively small NiO or NiMnO₃ particles. In contrast, a higher manganese content (Ni/Mn < 1) resulted in a considerable reduction in the level of metal dispersion and an increase in particle size of the metal.

The chemisorption of carbon monoxide is considered to be negligible for single-metal Mn/Al₂O₃ catalyst. In this case, it was assumed that CO adsorption occurs on Ni-containing samples. Thus, the data obtained from CO chemisorption were used to study the dispersion, specific surface area, and particle size of nickel-containing particles (Table 6). Similar to the

Table 6. Dispersion, Specific Surface Area, and Particle Size Calculated for Nickel Particles Based on CO Chemisorption

catalyst	D (%)	SA (m ² /g)	d (nm)
Ni/Mn 12:0	10.8	77.2	8.7
Ni/Mn 10:2	10.9	77.7	8.7
Ni/Mn 8:4	7.3	52.5	12.8
Ni/Mn 6:6	7.5	53.7	12.5
Ni/Mn 4:8	6.5	46.6	14.5
Ni/Mn 2:10	7.1	51.1	13.2
Ni/Mn 0:12	N/A	N/A	N/A

values calculated from H₂ chemisorption for overall metal particles, the dispersion and specific surface area decreased while the metal particle size increased with decreasing Ni/Mn ratio. However, it was found that by increasing the Mn content in the catalysts, the properties of the nickel particles narrowed to a smaller particle size range compared to those calculated for overall metal particles on each sample.

Catalysts' activity and selectivity with different active metals (single metal and alloys) for CO_x hydrogenation have been investigated by CO and H₂ chemisorption. It has been reported that the ratio of chemisorbed CO/H₂ correlates with activity and selectivity toward C₂₊ hydrocarbons.^{12,13,77} Figure 7 illustrates the changes in the ratio of chemisorbed CO/H₂ over catalysts with different nickel and manganese contents. It was found that the addition of manganese changed the CO/H₂ ratio. By increasing the Mn content (Ni/Mn < 5), the CO/H₂ ratio reduced for most samples. The correlation between a change in CO/H₂ and C₂₊ selectivity due to intimate metal–metal interactions has been shown by other researchers.⁷⁸ The two samples with the highest manganese content (Ni/Mn = 0.2 and 0) and the lowest activity for CO and CO₂ hydrogenation also had the lowest CO/H₂ ratio. It was found that the addition of manganese most likely leads to the adsorption of CO in bridge-type configuration. The changes in CO/H₂ chemisorption have been shown to affect the chain growth step during the CO_x hydrogenation. It is not possible to clearly explain the changes in activity and selectivity by only studying the CO/H₂ ratio. This is possibly due to the presence of different particle types (crystals), which was confirmed by both XRD and TPR patterns.

Density Functional Theory (DFT) Calculations. To investigate the effect of the Mn promoter on an atomic level, we used DFT to first explore the relative stability of various Mn-promoted Ni configurations under reducing conditions. Stabilities were ordered according to the chemical potential per Mn atom, as described in the Methods section and expressed as a function of H₂O partial pressure, while keeping the H₂ pressure fixed at the experimental ~0.5 bar. We tested a large number of structural configurations including substitution of Mn at a Ni(111) terrace and Ni(211) step and step edge sites, as well as the formation of MnO-like structures on Ni(111) terraces with different O and H terminations (see Figure S10 in the Supporting Information). Figure 8 shows the relative

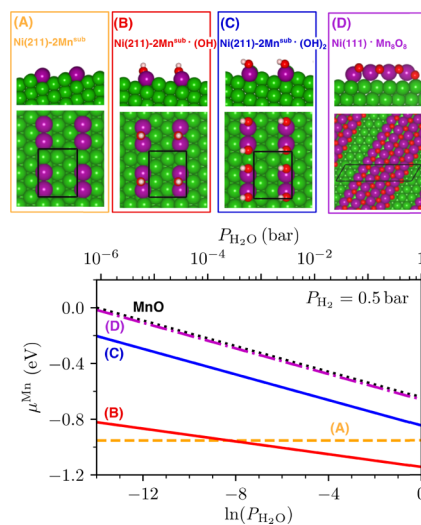


Figure 8. Phase diagram showing the relative stability per Mn atom (eV) for different Mn-promoted Ni configurations as a function of H₂O partial pressure under reducing conditions. The black dotted line signifies bulk MnO, while lines (A)–(D) correspond to four representative configurations whose DFT-optimized structures are shown in the panels above (side and top view). (Color map: green—nickel; purple—manganese; red—oxygen; white—hydrogen).

stability for few representative sampled structures within a realistic range for the H_2O pressure under operating conditions. Bulk MnO is represented by the dotted black line, and all of the data below this line suggest thermodynamically favorable surface wetting. Our analysis shows Mn atoms substituting the Ni(211) step edge sites to be most stable. This occurs preferentially in pairs to form two neighboring Mn substitutions as shown in the DFT-optimized structures in Figure 8A,B. Comparing the thermodynamic stabilities of these configurations suggests that less reducing conditions ($P_{\text{H}_2\text{O}} > 10^{-4}$ bar) favor an OH termination bridging the two neighboring Mn. Addition of a second OH group (panel (C)), however, is predicted to be less favorable. Our analysis further reveals that MnO-like structures such as MnO overlayer stripes (Figure 8D) and other MnO clusters (see Figure S10 in the Supporting Information) are considerably less stable than Mn-substituted slab configurations. This finding was strengthened by DFT calculations, which included a Hubbard + U correction to more accurately describe the oxide state. Investigating MnO configurations with different O-terminations and levels of hydrogenation consistently gave rise to a >0.7 eV higher chemical potential per Mn atom compared to the most stable Mn substitution at the Ni(211) B5 step edge site within the considered H_2O partial pressure range (see Figure S11 in the Supporting Information). However, under Mn-rich conditions, growth of such MnO-like surfaces could still be expected.

C–O activation is a crucial step in the conversion of CO and CO_2 to methane and C_{2+} hydrocarbons and often considered to be the rate-limiting step under reaction conditions.⁷⁹ In the direct CO dissociation pathway, CO^* undergoes direct C–O scission and forms atomic C^* and O^* adsorbates. The C^* species then hydrogenate and couple toward higher C species, while O^* hydrogenates to form water. Direct CO dissociation is a difficult step on Ni(111) terraces and therefore kinetically not preferred. Reactive Ni(211) steps were thus considered to dominate in terms of catalytic activity and used to demonstrate the effect of Mn promotion. Figure 9 shows the DFT-calculated Gibbs free reaction enthalpies for CO adsorption at the clean Ni(211) and at the two Mn-substituted Ni(211) configurations which were found most stable according to Figure 8. On the clean Ni(211) surface, CO^* binds at a B5 step edge site with an adsorption energy of -0.75 eV. This value is very similar to the -0.82 eV energy predicted for CO^* binding in the presence of two neighboring Mn substitution atoms at the B5 step edge (cf. structure panels in Figure 9). The difference in stability for the dissociated states, however, is considerably different. Here, we found that C^* binds on the B5 step site, while atomic O^* binds on the hollow site next to the step edge where it can be strongly stabilized by the presence of Mn due to the affinity of the latter toward oxidation. As a result, the Gibbs free reaction enthalpy for CO dissociation on clean Ni(211) step sites was predicted to be endothermic by 0.71 eV, while the corresponding process at the Mn-modified surface was found to be exothermic by -0.21 eV. This strong thermodynamic preference clearly demonstrates the enhanced activity for CO dissociation in the presence of Mn. We note that while Mn substitution at Ni(111) surface sites was predicted to be stable (see Figure S10 in the Supporting Information), its effect in promoting CO dissociation was predicted to be practically negligible (see Figure S12 in the Supporting Information). Growth of MnO-like surfaces at the

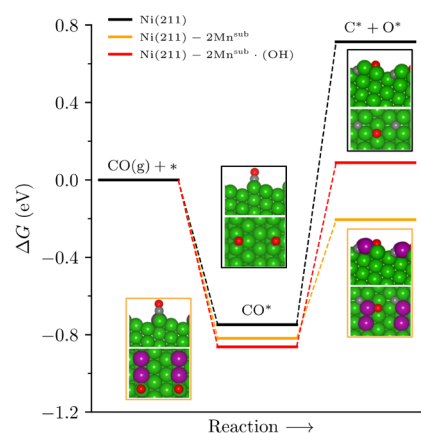


Figure 9. Gibbs free reaction energies (eV) for CO molecular adsorption and dissociation on a clean Ni(211) surface (in black) and for two Mn-promoted Ni(211) configurations, which were predicted as most stable and include two neighboring Mn substitutions at the B5 step edge with (in red) and without (in orange) a bridging OH termination between the two Mn atoms. The corresponding DFT-optimized structures are shown in the panels (side and top view). (Color map: green—nickel; purple—manganese; red—oxygen; white—hydrogen; carbon—gray).

steps⁸⁰ could block the active Ni(211) sites, leading to a reduced catalytic activity at higher Mn concentrations.

CONCLUSIONS

In summary, it is shown that the addition of manganese to the Ni/ Al_2O_3 catalyst significantly altered its catalytic performance for hydrogenation of CO and CO_2 in the presence of light hydrocarbons. Adding manganese to Ni/ Al_2O_3 also enhanced the selectivity of C_2 – C_4 production. However, there is an optimum amount of Mn added to the primary catalyst, which enhanced the catalyst activity and selectivity. The more hydrogen amount in the feed stream improved the catalyst activity for CO_x hydrogenation and selectivity toward C_2 – C_4 production in a temperature window (ca. 210–270 °C). Increasing the catalyst bed temperature beyond this narrow temperature window leads to a dramatic decrease in the concentration of C_2 – C_4 hydrocarbons, with a concomitant increase in methane concentration in the product stream. This suggests that possibly the cracking of higher hydrocarbons to methane is the dominant route at higher temperatures. The presence of a bimetallic oxide for catalysts with a Ni/Mn ratio more than 1 was found from XRD patterns. Furthermore, the TPR profile showed a single reduction peak in the low temperature range compared to single-metal Mn/ Al_2O_3 catalyst. The NO-FTIR investigation indicated the changes in the number of C- and O-accepting sites. Addition of optimum amount of Mn resulted in an increase of the O-accepting sites, which enhanced the CO dissociation. DFT calculation showed that the surface C^* and O^* are more stabilized over Mn-promoted catalysts. This resulted in a higher activity for CO hydrogenation (more C–O bond cleavage) and formation of more surface CH_x species. In addition, decreasing the C-/O-accepting ratio inhibited the C–C bond rupture, and thus less C_{2+} hydrocarbons were cracked to form methane.

■ ASSOCIATED CONTENT

S Supporting Information

The Supporting Information is available free of charge at <https://pubs.acs.org/doi/10.1021/acscatal.9b04863>.

Experimental and theoretical results; selectivity of C2–C4 hydrocarbons; Arrhenius plots for CO and CO₂ hydrogenation, and C₂H₆ hydrocracking; phase diagram showing the relative stability per Mn atom (eV); and Gibbs free reaction energies (eV) for molecular CO adsorption and dissociation (PDF)

■ AUTHOR INFORMATION

Corresponding Author

*E-mail: michael.stockenhuber@newcastle.edu.au.

ORCID 

Vahid Shadravan: 0000-0002-7392-4998

Vanessa J. Bukas: 0000-0002-0105-863X

G. T. Kasun Kalhara Gunasooriya: 0000-0003-1258-7841

Eric Kennedy: 0000-0001-7681-5220

Michael Stockenhuber: 0000-0001-5026-2218

Present Address

^{||}Department of Physics, Technical University of Denmark, 2800 Kongens Lyngby, Denmark (V.S.)

Notes

The authors declare no competing financial interest.

■ ACKNOWLEDGMENTS

V.J.B. acknowledges support from the H. C. Ørsted COFUND program (project no. 20932). G.T.K.K.G. acknowledges support from the Toyota Research Institute.

■ REFERENCES

- (1) Rönsch, S.; Schneider, J.; Matthischke, S.; Schlüter, M.; Götz, M.; Lefebvre, J.; Prabhakaran, P.; Bajohr, S. Review on methanation—From fundamentals to current projects. *Fuel* **2016**, *166*, 276–296.
- (2) Dry, M. E.; Hoogendoorn, J. C. Technology of the Fischer-Tropsch Process. *Catal. Rev.* **1981**, *23*, 265–278.
- (3) Sabatier, P.; Senderens, J. B. New methane synthesis. *C. R. Acad. Sci. Paris* **1902**, *134*, 514–516.
- (4) Dalai, A. K.; Davis, B. H. Fischer–Tropsch synthesis: A review of water effects on the performances of unsupported and supported Co catalysts. *Appl. Catal., A* **2008**, *348*, 1–15.
- (5) Hu, B.; Frueh, S.; Garces, H. F.; Zhang, L.; Aindow, M.; Brooks, C.; Kreidler, E.; Suib, S. L. Selective hydrogenation of CO₂ and CO to useful light olefins over octahedral molecular sieve manganese oxide supported iron catalysts. *Appl. Catal., B* **2013**, *132–133*, 54–61.
- (6) Gao, J.; Wang, Y.; Ping, Y.; Hu, D.; Xu, G.; Gu, F.; Su, F. A thermodynamic analysis of methanation reactions of carbon oxides for the production of synthetic natural gas. *RSC Adv.* **2012**, *2*, 2358–2368.
- (7) Razzaq, R.; Li, C.; Zhang, S. Coke oven gas: Availability, properties, purification, and utilization in China. *Fuel* **2013**, *113*, 287–299.
- (8) Lunsford, J. H. Catalytic conversion of methane to more useful chemicals and fuels: A challenge for the 21st century. *Catal. Today* **2000**, *63*, 165–174.
- (9) Dry, M. E. FT Catalysts. In *Studies in Surface Science and Catalysis*; Elsevier, 2004; Vol. 152, pp 533–600.
- (10) Mills, G. A.; Steffgen, F. W. Catalytic methanation. *Catal. Rev.* **1974**, *8*, 159–210.
- (11) Enger, B. C.; Holmen, A. Nickel and Fischer-Tropsch Synthesis. *Catal. Rev.* **2012**, *54*, 437–488.
- (12) Ishihara, T.; Horiuchi, N.; Inoue, T.; Eguchi, K.; Takita, Y.; Arai, H. Effect of alloying on CO hydrogenation activity over SiO₂-supported CO-Ni alloy catalysts. *J. Catal.* **1992**, *136*, 232–241.
- (13) Vannice, M. A.; Garten, R. L. Metal-support effects on the activity and selectivity of Ni catalysts in COH₂ synthesis reactions. *J. Catal.* **1979**, *56*, 236–248.
- (14) Kao, C. C.; Tsai, S. C.; Chung, Y. W. Surface electronic properties and CO hydrogenation activity of nickel deposited on rutile TiO₂(100) as a model supported catalyst. *J. Catal.* **1982**, *73*, 136–146.
- (15) Bartholomew, C. H.; Pannell, R. B.; Butler, J. L.; Mustard, D. G. Nickel-support interactions: Their effects on particle morphology, adsorption, and activity selectivity properties. *Ind. Eng. Chem. Prod. Res. Dev.* **1981**, *20*, 296–300.
- (16) Ishihara, T.; Eguchi, K.; Arai, H. Hydrogenation of carbon monoxide over SiO₂-supported Fe-Co, Co-Ni and Ni-Fe bimetallic catalysts. *Appl. Catal.* **1987**, *30*, 225–238.
- (17) Bezemer, G. L.; Radstake, P. B.; Falke, U.; Oosterbeek, H.; Kuipers, H. P. C. E.; van Dillen, A. J.; de Jong, K. P. Investigation of promoter effects of manganese oxide on carbon nanofiber-supported cobalt catalysts for Fischer–Tropsch synthesis. *J. Catal.* **2006**, *237*, 152–161.
- (18) Shadravan, V.; Kennedy, E.; Stockenhuber, M. An experimental investigation on the effects of adding a transition metal to Ni/Al₂O₃ for catalytic hydrogenation of CO and CO₂ in presence of light alkanes and alkenes. *Catal. Today* **2018**, *307*, 277–285.
- (19) Seok, S.-H.; Han, S. H.; Lee, J. S. The role of MnO in Ni/MnO-Al₂O₃ catalysts for carbon dioxide reforming of methane. *Appl. Catal., A* **2001**, *215*, 31–38.
- (20) Zhao, K.; Li, Z.; Bian, L. CO₂ methanation and co-methanation of CO and CO₂ over Mn-promoted Ni/Al₂O₃ catalysts. *Front. Chem. Sci. Eng.* **2016**, *10*, 273–280.
- (21) Lohitharn, N.; Goodwin, J. G. Impact of Cr, Mn and Zr addition on Fe Fischer–Tropsch synthesis catalysis: Investigation at the active site level using SSITKA. *J. Catal.* **2008**, *257*, 142–151.
- (22) Zhao, A.; Ying, W.; Zhang, H.; Hongfang, M.; Fang, D. Ni/Al₂O₃ catalysts for syngas methanation: Effect of Mn promoter. *J. Nat. Gas Chem.* **2012**, *21*, 170–177.
- (23) Arrhenius, S. Über die Dissociationswärme und den Einfluss der Temperatur auf den Dissociationsgrad der Elektrolyte. *Z. Phys. Chem.* **1889**, *4*, 96.
- (24) Ghoorah, M.; Dlugogorski, B. Z.; Oskierski, H. C.; Kennedy, E. M. Study of thermally conditioned and weak acid-treated serpentinites for mineralisation of carbon dioxide. *Miner. Eng.* **2014**, *59*, 17–30.
- (25) Degen, T.; Sadki, M.; Bron, E.; König, U.; Nénert, G. The HighScore suite. *Powder Diffraction*. **2014**, *29*, S13–S18.
- (26) Match! - Phase Identification from Powder Diffraction, Crystal Impact-Dr. H. Putz & Dr. K. Brandenburg GbR, Kreuzherrenstr. 102, 53227 Bonn, Germany.
- (27) Velu, S.; Gangwal, S. K. Synthesis of alumina supported nickel nanoparticle catalysts and evaluation of nickel metal dispersions by temperature programmed desorption. *Solid State Ionics* **2006**, *177*, 803–811.
- (28) Hammer, B.; Hansen, L. B.; Nørskov, J. K. Improved adsorption energetics within density-functional theory using revised Perdew-Burke-Ernzerhof functionals. *Phys. Rev. B* **1999**, *59*, 7413–7421.
- (29) Kresse, G.; Joubert, D. From ultrasoft pseudopotentials to the projector augmented-wave method. *Phys. Rev. B* **1999**, *59*, 1758–1775.
- (30) Kresse, G.; Furthmüller, J. Efficient iterative schemes for ab initio total-energy calculations using a plane-wave basis set. *Phys. Rev. B* **1996**, *54*, 11169–11186.
- (31) Kresse, G.; Furthmüller, J. Efficiency of ab-initio total energy calculations for metals and semiconductors using a plane-wave basis set. *Comput. Mater. Sci.* **1996**, *6*, 15–50.
- (32) Wang, L.; Maxisch, T.; Ceder, G. Oxidation energies of transition metal oxides within the GGA+U. *Phys. Rev. B* **2006**, *73*, No. 195107.

- (33) Monkhorst, H. J.; Pack, J. D. Special points for Brillouin-zone integrations. *Phys. Rev. B* **1976**, *13*, 5188–5192.
- (34) Habazaki, H.; Yamasaki, M.; Zhang, B. P.; Kawashima, A.; Kohno, S.; Takai, T.; Hashimoto, K. Co-methanation of carbon monoxide and carbon dioxide on supported nickel and cobalt catalysts prepared from amorphous alloys. *Appl. Catal., A* **1998**, *172*, 131–140.
- (35) Kester, K. B.; Zagli, E.; Falconer, J.L. Methanation of carbon monoxide and carbon dioxide on Ni/Al₂O₃ catalysts: effects of nickel loading. *Appl. Catal.* **1986**, *22*, 311–319.
- (36) Fujita, Si.; Nakamura, M.; Doi, T.; Takezawa, N. Mechanisms of methanation of carbon dioxide and carbon monoxide over nickel/alumina catalysts. *Appl. Catal., A* **1993**, *104*, 87–100.
- (37) Littlewood, P.; Xie, X.; Bernicke, M.; Thomas, A.; Schomäcker, R. Ni_{0.05}Mn_{0.95}O catalysts for the dry reforming of methane. *Catal. Today* **2015**, *242*, 111–118.
- (38) Gottschalk, F. M.; Hutchings, G. J. Manganese oxide water–gas shift catalysts initial optimization studies. *Appl. Catal.* **1989**, *51*, 127–139.
- (39) Liu, Q.; Gao, J.; Gu, F.; Lu, X.; Liu, Y.; Li, H.; Zhong, Z.; Liu, B.; Xu, G.; Su, F. One-pot synthesis of ordered mesoporous Ni–V–Al catalysts for CO methanation. *J. Catal.* **2015**, *326*, 127–138.
- (40) Lu, X.; Gu, F.; Liu, Q.; Gao, J.; Liu, Y.; Li, H.; Jia, L.; Xu, G.; Zhong, Z.; Su, F. VOx promoted Ni catalysts supported on the modified bentonite for CO and CO₂ methanation. *Fuel Process. Technol.* **2015**, *135*, 34–46.
- (41) Sehested, J.; Dahl, S.; Jacobsen, J.; Rostrup-Nielsen, J. R. Methanation of CO over nickel: Mechanism and kinetics at high H₂/CO ratios. *J. Phys. Chem. B* **2005**, *109*, 2432–2438.
- (42) Liu, Q.; Gu, F.; Lu, X.; Liu, Y.; Li, H.; Zhong, Z.; Xu, G.; Su, F. Enhanced catalytic performances of Ni/Al₂O₃ catalyst via addition of V₂O₃ for CO methanation. *Appl. Catal., A* **2014**, *488*, 37–47.
- (43) Peebles, D. E.; Goodman, D. W.; White, J. M. Methanation of carbon dioxide on Ni(100) and the effects of surface modifiers. *J. Phys. Chem. A* **1983**, *87*, 4378–4387.
- (44) Hubble, R. A.; Lim, J. Y.; Dennis, J. S. Kinetic studies of CO₂ methanation over a Ni/[gamma]-Al₂O₃ catalyst. *Faraday Discuss.* **2016**, *192*, 529–544.
- (45) Anderson, J. R.; Baker, B. G. The Hydrocracking of Saturated Hydrocarbons Over Evaporated Metal Films. *Proc. R. Soc. London, Ser. A* **1963**, *271*, 402–423.
- (46) Zeigarnik, A. V.; Valdés-Pérez, R. E.; Myatkovskaya, O. N. C–C Bond Scission in Ethane Hydrogenolysis. *J. Phys. Chem. B* **2000**, *104*, 10578–10587.
- (47) Goodman, D. W. Ethane hydrogenolysis over single crystals of nickel: Direct detection of structure sensitivity. *Surf. Sci.* **1982**, *123*, L679–L685.
- (48) Pandey, D.; Deo, G. Promotional effects in alumina and silica supported bimetallic Ni–Fe catalysts during CO₂ hydrogenation. *J. Mol. Catal. A: Chem.* **2014**, *382*, 23–30.
- (49) Zhou, R.-S.; Snyder, R. L. Structures and transformation mechanisms of the [eta], [gamma] and [theta] transition aluminas. *Acta Crystallogr., Sect. B: Struct. Sci.* **1991**, *47*, 617–630.
- (50) Cairns, R. W.; Ott, E. X-Ray Studies of the System Nickel–Oxygen–Water. I. Nickelous Oxide and Hydroxide. *J. Am. Chem. Soc.* **1933**, *55*, 527–533.
- (51) Roelofsen, J. N.; Peterson, R. C.; Raudsepp, M. Structural variation in nickel aluminate spinel (NiAl₂O₄). *Am. Mineral.* **1992**, *77*, 522–528.
- (52) Cloud, W. H. Crystal structure and ferrimagnetism in NiMnO₃ and CoMnO₃. *Phys. Rev.* **1958**, *111*, 1046–1049.
- (53) Huang, L.; Zhang, F.; Chen, R.; Hsu, A. T. Manganese-promoted nickel/alumina catalysts for hydrogen production via auto-thermal reforming of ethanol. *Int. J. Hydrogen Energy* **2012**, *37*, 15908–15913.
- (54) Norrestam, R.; Ingri, N.; Östlund, E.; Bloom, G.; Hagen, G. Alpha-manganese(III) oxide - a C-type sesquioxide of orthorhombic symmetry. *Acta Chem. Scand.* **1967**, *21*, 2871–2884.
- (55) Kondrashev, Y. D.; Zaslavskii, A. I. The structure of the modifications of manganese oxide. *Izv. Akad. Nauk SSSR, Ser. Fiz.* **1951**, *15*, 179–186.
- (56) Hu, D.; Gao, J.; Ping, Y.; Jia, L.; Gunawan, P.; Zhong, Z.; Xu, G.; Gu, F.; Su, F. Enhanced investigation of CO methanation over Ni/Al₂O₃ catalysts for synthetic natural gas production. *Ind. Eng. Chem. Res.* **2012**, *51*, 4875–4886.
- (57) Guo, C.; Wu, Y.; Qin, H.; Zhang, J. CO methanation over ZrO₂/Al₂O₃ supported Ni catalysts: A comprehensive study. *Fuel Process. Technol.* **2014**, *124*, 61–69.
- (58) Rynkowski, J. M.; Paryjczak, T.; Lenik, M. On the nature of oxidic nickel phases in NiO/ γ -Al₂O₃ catalysts. *Appl. Catal., A* **1993**, *106*, 73–82.
- (59) Yang, J.; Wang, X.; Li, L.; Shen, K.; Lu, X.; Ding, W. Catalytic conversion of tar from hot coke oven gas using 1-methylnaphthalene as a tar model compound. *Appl. Catal., B* **2010**, *96*, 232–237.
- (60) Zhao, A.; Ying, W.; Zhang, H.; Ma, H.; Fang, D. Ni–Al₂O₃ catalysts prepared by solution combustion method for syngas methanation. *Catal. Commun.* **2012**, *17*, 34–38.
- (61) Pozan, G. S. Effect of support on the catalytic activity of manganese oxide catalysts for toluene combustion. *J. Hazard. Mater.* **2012**, *221*–222, 124–130.
- (62) Gutiérrez-Ortiz, J. I.; López-Fonseca, R.; Aurrekoetxea, U.; González-Velasco, J. R. Low-temperature deep oxidation of dichloromethane and trichloroethylene by H-ZSM-5-supported manganese oxide catalysts. *J. Catal.* **2003**, *218*, 148–154.
- (63) Tang, Q.; Huang, X.; Wu, C.; Zhao, P.; Chen, Y.; Yang, Y. Structure and catalytic properties of K-doped manganese oxide supported on alumina. *J. Mol. Catal. A: Chem.* **2009**, *306*, 48–53.
- (64) Bhargava, S. K.; Akolekar, D. B. Adsorption of NO and CO over transition-metal-incorporated mesoporous catalytic materials. *J. Colloid Interface Sci.* **2005**, *281*, 171–178.
- (65) Hadjiivanov, K. I. Identification of Neutral and Charged N_xO_y Surface Species by IR Spectroscopy. *Catal. Rev.* **2000**, *42*, 71–144.
- (66) Harrison, P. G.; Thornton, E. W. Tin oxide surfaces. Part 9.-Infrared study of the adsorption of CO, NO and CO + NO mixtures on tin(IV) oxide gels containing ion-exchanged Cr^{III}, Mn^{II}, Fe^{III}, Co^{II}, Ni^{II} and Cu^{II}. *J. Chem. Soc., Faraday Trans. 1* **1978**, *74*, 2703–2713.
- (67) Platero, E. E.; Fubini, B.; Zecchina, A. Nitric oxide adsorption on NiO: An infrared and calorimetric study. *Surf. Sci.* **1987**, *179*, 404–424.
- (68) Zecchina, A.; Scarano, D.; Bordiga, S.; Ricchiardi, G.; Spoto, G.; Geobaldo, F. IR studies of CO and NO adsorbed on well characterized oxide single microcrystals. *Catal. Today* **1996**, *27*, 403–435.
- (69) Mihaylov, M.; Hadjiivanov, K.; Abadjieva, N.; Klissurski, D.; Mintchev, L. Characterization of Zirconia-supported Nickel Catalysts Prepared by Multiple Ion-exchange. *Stud. Surf. Sci. Catal.* **1998**, *118*, 295–304.
- (70) Atanasova, P.; Agudo, A. L. Infrared studies of nitric oxide adsorption on reduced and sulfided P-Ni-Mo/Al₂O₃ catalysts. *Appl. Catal., B* **1995**, *5*, 329–341.
- (71) Peri, J. B. Infrared studies of Ni held at low concentrations on alumina supports. *J. Catal.* **1984**, *86*, 84–94.
- (72) Tanaka, T.; Okuhara, T.; Misono, M. Intermediacy of organic nitro and nitrite surface species in selective reduction of nitrogen monoxide by propene in the presence of excess oxygen over silica-supported platinum. *Appl. Catal., B* **1994**, *4*, L1–L9.
- (73) Spoto, G.; Bordiga, S.; Scarano, D.; Zecchina, A. Well defined CuI(NO), CuI(NO)₂ and CuII(NO)X (X = O⁻ and/or NO₂⁻) complexes in CuI-ZSMS prepared by interaction of H-ZSMS with gaseous CuCl. *Catal. Lett.* **1992**, *13*, 39–44.
- (74) Aylor, A. W.; Larsen, S. C.; Reimer, J. A.; Bell, A. T. An Infrared Study of NO Decomposition over Cu-ZSM-5. *J. Catal.* **1995**, *157*, 592–602.
- (75) Nakamoto, K. Theory of Normal Vibrations. In *Infrared and Raman Spectra of Inorganic and Coordination Compounds*; John Wiley & Sons, Inc, 2008; pp 1–147.

(76) Crabtree, R. H. General Properties of Organometallic Complexes. In *The Organometallic Chemistry of the Transition Metals*; John Wiley & Sons, Inc, 2005; pp 29–52.

(77) Rodriguez-Ramos, I.; Guerrero-Ruiz, A.; Fierro, J. L. G. Effect of oxide promoters on the surface characteristics of carbon-supported Co and Ru catalysts. *App. Surf. Sci.* **1989**, *40*, 239–247.

(78) Das, P. C.; Pradhan, N. C.; Dalai, A. K.; Bakhshi, N. N. Carbon monoxide hydrogenation over various titania-supported Ru–Ni bimetallic catalysts. *Fuel Process. Technol.* **2004**, *85*, 1487–1501.

(79) Studt, F.; Sharafutdinov, I.; Abild-Pedersen, F.; Elkjær, C. F.; Hummelshøj, J. S.; Dahl, S.; Chorkendorff, I.; Nørskov, J. K. Discovery of a Ni–Ga catalyst for carbon dioxide reduction to methanol. *Nat. Chem.* **2014**, *6*, 320.

(80) Bechstein, R.; Kristoffersen, H. H.; Vilhelmsen, L. B.; Rieboldt, F.; Stausholm-Møller, J.; Wendt, S.; Hammer, B.; Besenbacher, F. Packing Defects into Ordered Structures: Strands on TiO₂. *Phys. Rev. Lett.* **2012**, *108*, No. 236103.